PAPER

Check for updates

Hydrogen production by graphdiyne (C$_n$H$_{2n-2}$)-based graphdiyne/CuI/NiMn(LDHs) double S-scheme heterojunctions

Zhenkun Liu and Zhiliang Jin (iD) *

Graphdiyne (GDY), as the latest carbon material, has demonstrated exceptional performance in a number of applications. The good conduction performance of GDY may promote the electron transfer and greatly improve the low separation rate of electron–hole pairs caused by the slow electron transfer rate. Herein, CuI–GDY was obtained by the cross-coupling method, and CuI–GDY/NiMn(LDHs) composite catalysts were obtained by a simple solvothermal method. The lamellar structure of NiMn(LDHs) is endowed with a large specific surface area and a rough surface. The double S-scheme heterojunctions constructed between the composite catalysts accelerates the electron transfer rate, allowing more photogenerated electrons to participate in the hydrogen precipitation reaction. The good stability of GDY is brought to the composite catalyst after compounding and makes the hole–electron pair compounding rate of the composite catalyst decrease. Thus, the composite catalysts maintained good hydrogen precipitation activity even after 20 hours of cycling, and the hydrogen precipitation activity was further improved. The hydrogen production activity of the composite catalyst (1094.6 μmol g^{-1} h^{-1}) was increased by 11.24, 8.80, 20.99, 3.78 and 2.58 times when compared to pure GDY, CuI–GDY, CuI, NiMn(LDHs) and NiMn(LDHs)–CuI, respectively. Furthermore, NiMn(LDHs)-x in the dye sensitization system shows strong stability. This work provides a new perspective for GDY modification on semiconductor bandgap and the application of GDY in the photocatalytic hydrogen generation reaction.

1. Introduction

It is well known that traditional fossil fuel is unrenewable.[1,2] With the increasing detrimental growth of the global greenhouse effect, it is critical to seek clean energy to replace fossil energy. As the cleanest energy, hydrogen is undoubtedly the best choice.[3–6] However, hydrogen production from water cracking requires a huge energy amount in kinetics to break the barrier. Thus, efficient, stable and economical photocatalysts are needed to reduce the activation energy to produce hydrogen.[7–9] Among them, non-metallic carbon-based materials are very attractive because of their environmental friendliness, abundance, diversity and low cost. One of the most representative examples is graphitic carbon nitride, which has received wide attention for its simple synthesis, stable structure and chemical properties, and wide range of light absorption.[10,11] However, it also has obvious drawbacks, exhibiting poor photocatalytic performance due to the low utilization of sunlight and rapid compounding of photoexcited carriers.[12,13] Similarly, other photocatalysts tend to have some disadvantages, such as an electron–hole complexation that is too fast and band gaps that are too narrow or wide.[14–17] To solve these drawbacks, techniques such as constructing heterojunctions,[18,19] metal doping, and nonmetal modification can often be used to suppress drawbacks, such as electron–hole pair complexation. Thus, the photocatalyst is built towards better photocatalytic hydrogen evolution activity.[20,21] In recent years, S-scheme heterojunctions have been of increasing interest.[22,23] This is because when S-scheme heterojunctions are established between different catalysts, a built-in electric field is formed inside the catalyst. The built-in electric field, Coulomb force and band edge bending at the catalyst interface will induce more useful electrons to participate in the reduction reaction.[24]

As a new member of carbon materials, GDY is composed of sp and sp^2 hybrid carbon networks. It can be as thin as a single atomic layer, particularly when it was first synthesized chemically *in situ* on copper foil by the Li group in 2010.[25–27] Due to the properties of GDY itself, such as abundant chemical bonding, high conjugation, oversized π structure and high electron mobility, it has great potential in the fields of catalysis, electricity, optics, and information.[16,25]

School of Chemistry and Chemical Engineering, Ningxia Key Laboratory of Solar Chemical Conversion Technology, Key Laboratory for Chemical Engineering and Technology, State Ethnic Affairs Commission, North Minzu University, Yinchuan, 750021, P. R. China. E-mail: zl-jin@nun.edu.cn

GDY has unlimited generation space and can be grown on any substrate. The Li group has successfully constructed graphitylene nanowires with high-quality defect-free surfaces using the VLS growth process.[28] Wang, Li and coworkers reported a novel sp-hybridized nitrogen-doped ultrathin GDY as a metal-free catalyst applied in the oxygen reduction reaction.[29] However, there are few applications of GDY in the field of photocatalysis. Of note is the innovation in the synthesis method of GDY. In this paper, we used CuI instead of the traditional copper foil as a carrier, and thus GDY containing CuI (CuI–GDY) was produced. Pure GDY itself has a narrow band gap, and hydrogen production requires a suitable band gap, conductivity band position and valence band position, so its hydrogen production activity is average. CuI is widely used in photocatalysis and coupling reactions in organic reactions because of its wide band gap and activity. CuI not only bridges the narrow band gap of GDY, but also promotes the coupling of alkyne groups and acts as a "crystal nucleus" for the growth of graphite alkynes in the preparation of CuI–GDY.

Because of its unique layer structure, high specific surface area, adjustable ratio composition, environmentally friendly quality and low expense, layered double hydroxides (LDHs) have been widely studied and have attracted great attention, especially in the fields of catalysis, energy storage and material science.[30–34] NiMn(LDHs) are non-precious metal-containing 2D materials that are widely used in supercapacitors due to their high conductivity and cycling stability, but there are few applications for its role in photocatalytic hydrogen production.[35–37] Drawing on the core–shell NiMn(LDHs) made by etching SiO_2 nanospheres as a substrate by the Li group, flake NiMn(LDHs) was made without the use of a substrate.[32]

In this paper, CuI–GDY was loaded on the surface of NiMn(LDHs) using a simple solvent heat method as planned. Compared with the pure catalyst, the double S-scheme heterojunctions constructed between the composite catalysts accelerates the electron transfer rate, allowing more photogenerated electrons to participate in the hydrogen precipitation reaction, and the introduction of GDY greatly increases the stability of the catalysts, thus enabling the composite catalysts to maintain good hydrogen precipitation activity even after 20 hours of cycling.

2. Experiment

2.1. Preparation of CuI–GDY and GDY

First, 4.3 mL ethynyltrimethylsilane was dissolved in a three-neck flask containing 35 mL tetrahydrofuran and protected with N_2. At −78 °C, 12 mL of n-butyllithium solution dissolved in tetrahydrofuran was added to the above solution slowly dropwise near the liquid surface, and stirred for 30 minutes. Then, 20 mL of anhydrous zinc chloride solution dissolved in tetrahydrofuran was added dropwise to the reaction with continuous stirring. After 30 minutes, it rose to room temperature, and 1.104 g hexabromobenzene, 500 mg tetrakis(triphenylphosphine)palladium(0) and 25 mL toluene

were added. The reaction was continued under an atmosphere of nitrogen at 80 °C for 3 days. After the reaction, 20 mL of 1 mol L^{-1} HCl was added to the system, which was separated by extraction with ethyl acetate. The bottom solution was removed and the top solution was washed. Then, it was dried with anhydrous sodium sulfate, concentrated to dry, separated and purified by eluent column chromatography with a mixture of n-hexane and dichloromethane (volume ratio 4:1) to obtain a pale yellow solid hexakis[(trimethylsilyl)ethynyl]benzene. The obtained intermediates were dissolved in 20 mL tetrahydrofuran, and 0.4 mL tetrabutylammonium fluoride solution was added under the protection of N_2. After continuous stirring for 10 minutes at 8 °C, extraction was carried out using ethyl acetate, washing with saturated brine, drying with anhydrous sodium sulfate, and concentrating and drying to obtain a black solid hexylenyl benzene. The black solid was dissolved with 25 mL of pyridine, and added dropwise under N_2 protection to a three-neck flask containing 50 mL of pyridine and 500 mg of CuI within 24 h. This process was performed at 60 °C. After drip-adding, the 2-days reaction was followed by concentration to dry to obtain CuI–GDY.[17,25] To obtain pure GDY, CuI–GDY was washed with ammonia to remove CuI acting as a "crystal nucleus" until the liquid was colorless. After oven drying, pure GDY was obtained (Fig. 1).

2.2. Preparation of NiMn(LDHs) and composite catalyst

First, 3 mmol of $Ni(NO_3)_2 \cdot 6H_2O$ and 1.5 mmol of $Mn(NO_3)_2$ were weighed into a three-mouth flask containing 100 mL of absolute ethanol, and stirred to disperse evenly. Under the atmosphere of N_2 and the water bath kept at 50 °C, 23 mL of ammonia (1 mol L^{-1}) was measured and added to the above solution dropwise, and the product was continuously stirred for one hour. The product was left to stand, washed with deionized water and ethanol, and then transferred to a vacuum-pressure desiccator for drying at 50 °C overnight.

A mass of 10 mg of GDY was weighed and added to a beaker containing 30 mL of anhydrous ethanol, and the mixture was uniformly dispersed by ultrasound. Then, 100 mg of NiMn(LDHs) was added to the above solution. The mixture was stirred for 1 hour for even dispersion, then steamed at 70 °C in a water bath until the solution was thick. Finally, the sample was transferred to a vacuum oven at 50 °C to dry. The mixed catalyst NiMn(LDHs)-10 was obtained, and other ratios of mixed catalyst NiMn(LDHs)-x (x = 5, 15, 20, and 25) were prepared using the same experimental procedure, with the only difference being the amount of CuI–GDY (Fig. 2).

2.3. Hydrogen production experiment

A photocatalytic hydrogen production experiment was carried out in a 65 mL glass bottle. A mass of 10 mg of catalyst powder and 10 mg of eosin Y water solution were weighed and added into 30 mL of aqueous triethanolamine (TEOA) solution (volume fraction: 15%). The mixture was sonicated to obtain an even dispersion, and N_2 was infused for three
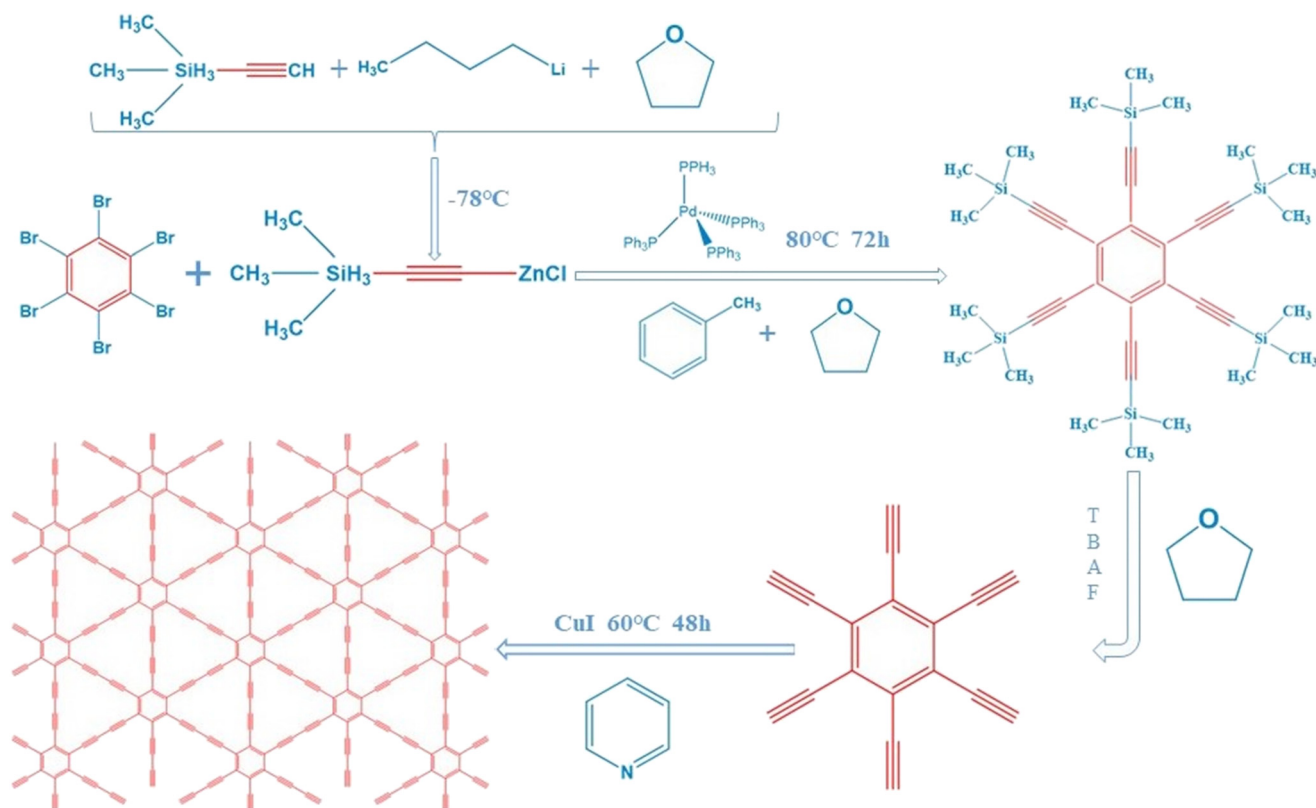
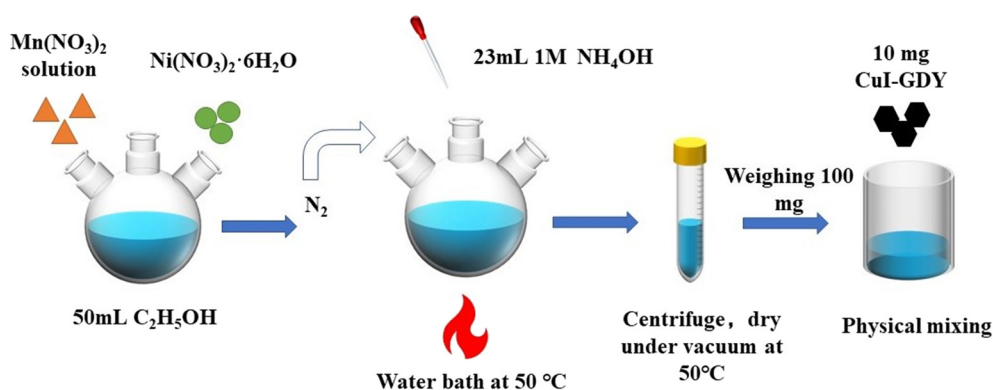Fig. 1 Schematic diagrams of the synthetic route for graphdiyne.

Fig. 2 Schematic diagrams of the synthetic route for NiMn(LDHs) and composite catalyst.

minutes to remove air from the bottle. The multi-channel photocatalytic reaction system with 5 W of white light was used to simulate the sunlight. For each time that 0.5 mL of gas was extracted from the bottle, the hydrogen content was detected by Tianmei GC7900 gas chromatography (TCD, 13X column, N_2 as carrier), and the hydrogen production was analyzed by the external standard method.

2.4. Instruments and medicines

The diffraction patterns of GDY, CuI–GDY, NiMn(LDHs) and NiMn(LDHs)/CuI–GDY were analyzed by X-ray diffractometer (XRD, Rigaku RINT-2000), with the test range and test speed set to 10–80° and 10° min^{-1}. The microscopic morphologies of GDY, CuI–GDY, NiMn(LDHs) and NiMn(LDHs)/CuI–GDY were studied using a scanning electron microscope (SEM, Zeiss Evo 10) and transmission electron microscope (TEM, Tecnai, G2-TF30). An UV-2550 (Shimadzu) spectrometer equipped with an integrating sphere was used to explore the visible light absorption of the samples between 250–800 nm. The photoluminescence spectral data of the material were recorded on the FLUOROMAX-4 spectrometer. The platinum electrode was used as the counter electrode, the calomel electrode was the reference electrode, and the sample was the working electrode for photoelectrochemical testing on the VersaStat4-400 electrochemical workstation. A 0.2 M

Na$_2$SO$_4$ solution was used as the electrolyte, and 300 W xenon lamp was used as the light source ($\lambda \geq 420$ nm cut-off filter). All drugs were analytically pure.

3. Results and discussion

3.1. XRD analysis

The crystallinity and crystal structure of CuI–GDY, GDY, CuI, NiMn(LDHs) and composite materials were analyzed by XRD. In Fig. 3(a), the peaks at 25.5°, 29.5°, 42.2° and 50.0° are attributed to the crystal faces (111), (200), (220) and (311) of CuI (PDF#75-832), respectively.[38] These four facets can be seen in CuI–GDY. Due to wear in the synthesis process, the peak type of CuI is reduced. However, compared with pure CuI, the peak type of CuI can still be seen. In Fig. 3(b), the resulting products of NiMn(LDHs) exhibit a series of crystal face (003), (006), (012) and (015) reflection peaks at 11.3°, 22.7°, 33.4°, and 34.4°, respectively, which are typical diffraction patterns of LDHs, indicating that LDHs were successfully prepared.[21] However, crystalline Mn$_3$O$_4$ appears in the composite due to partial oxidation, and the peak of CuI becomes obvious after the content of CuI–GDY increases. The success of the composite materials is illustrated.

3.2. Infrared and Raman analysis

Functional groups of GDY, NiMn(LDHs) and NiMn(LDHs)-20 were identified by infrared spectroscopy. As depicted in Fig. 4(a), the tensile vibration of the acetylene bond of GDY results in a peak of 2197.2 cm^{-1},[39] and stretching peaks of the aromatic ring skeleton appeared in the range of 1400–1600 cm^{-1}. The energy bands at 2336.5 and 2362.4 cm^{-1} are caused by the C=O bond stretching vibrational mode of CO$_2$, and the energy band at 1374.5 cm^{-1} is caused by the stretching vibration of the C–C/C–O bond.[40,41] The stretching vibration of the H–O bond in NiMn(LDHs) gives rise to the energy band at 3667.2 cm^{-1}, which is still very obvious in the composite catalyst. The tensile vibration of the N–O bond of NiMn(LDHs) results in a peak at 1383.6 cm^{-1}. Fig. 4(b) shows the Raman spectra of GDY. The characteristic peak at 1346.7 cm^{-1} corresponds to the G band of sp^2 carbon, which shows the interlayer stacking mode of carbon atoms in the sample. The characteristic peak at 1572.5 cm^{-1} may originate from the D band of the sp^2 carbon.[42] The vibration of the conjugated diyne chain (–C≡C–C≡C–) gives rise to the peaks at 1992.4 and 2140.4 cm^{-1}.

3.3. XPS analysis

To further prove the successful compounding of CuI–GDY and NiMn(LDHs), XPS analysis was separately carried out on GDY, CuI–GDY, NiMn(LDHs) and NiMn(LDHs)-20. The results are shown in Fig. 5(a), indicating that only NiMn(LDHs) and composite catalysts have both Ni and Mn elements. The composition and valence state of CuI–GDY were clarified. Fig. 5(b) shows the XPS spectrum of C 1s, fitting four peaks at 284.50, 284.88, 286.05 and 288.68 eV, representing the C–C(sp^2), C–C(sp), C–O and C=O bonds, respectively.[43] The peak area of sp is twice that of sp^2. Compared with pure GDY, all four peaks of C 1s in the composite catalyst are shifted to the high field, indicating that C loses electrons. Fig. 5(c) and (d) show spectrograms of Cu 2p at 933.00 and 952.70 eV, which correspond to Cu 2p$_{3/2}$ and Cu 2p$_{1/2}$, respectively.[44] Furthermore, the peaks at 619.47 and 631.15 eV were attributed to I 3d$_{5/2}$ and I 3d$_{3/2}$, respectively.[45] It can be seen that both Cu 2p and I 3d move to the high field. Fig. 5(e) is the spectrum of Ni 2p in NiMn(LDHs), corresponding to 856.18, 861.76, 874.06 and 880.03 eV. Ni moves to the low field after catalyst recombination, which indicates that Ni gets electrons. Fig. 5(f) is the spectrum of Mn 2p in NiMn(LDHs). The peaks at 643.70 and 656.17 eV correspond to Mn 2p$_{3/2}$ and Mn 2p$_{1/2}$, respectively. It can be seen that there is a small amount of oxidation state of Mn (Mn^{3+}).[32] Compared with the binding energy of the single catalyst, the composite catalyst shifts to different degrees, which proves the electron transfer between CuI, GDY and NiMn(LDHs).
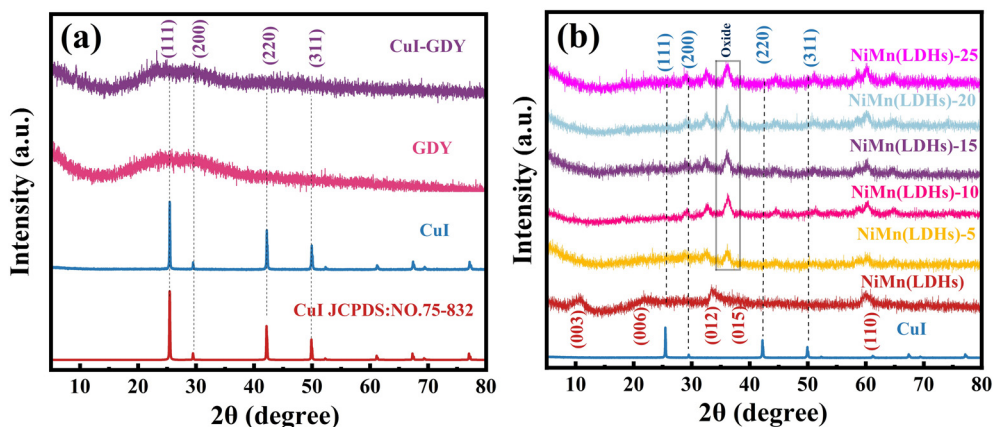

Fig. 3 XRD patterns of (a) CuI, CDY, CuI–GDY, (b) CuI, NiMn(LHDs)-*x* (*x* = 0, 5, 10, 15, 20 and 25).

This journal is © The Royal Society of Chemistry 2023

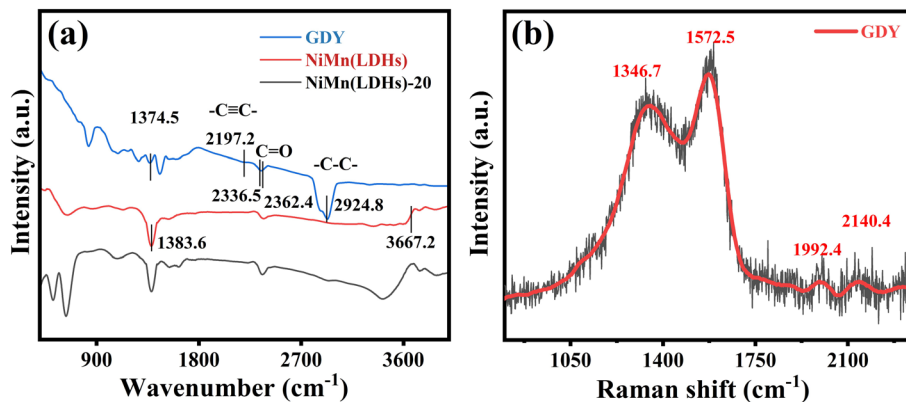*Catal. Sci. Technol.*, 2023, **13**, 1074–1086 | **1077**

Fig. 4 (a) FT-IR spectra of GDY, NiMn(LDHs), and NiMn(LDHs)-20. (b) Raman spectrum of GDY.
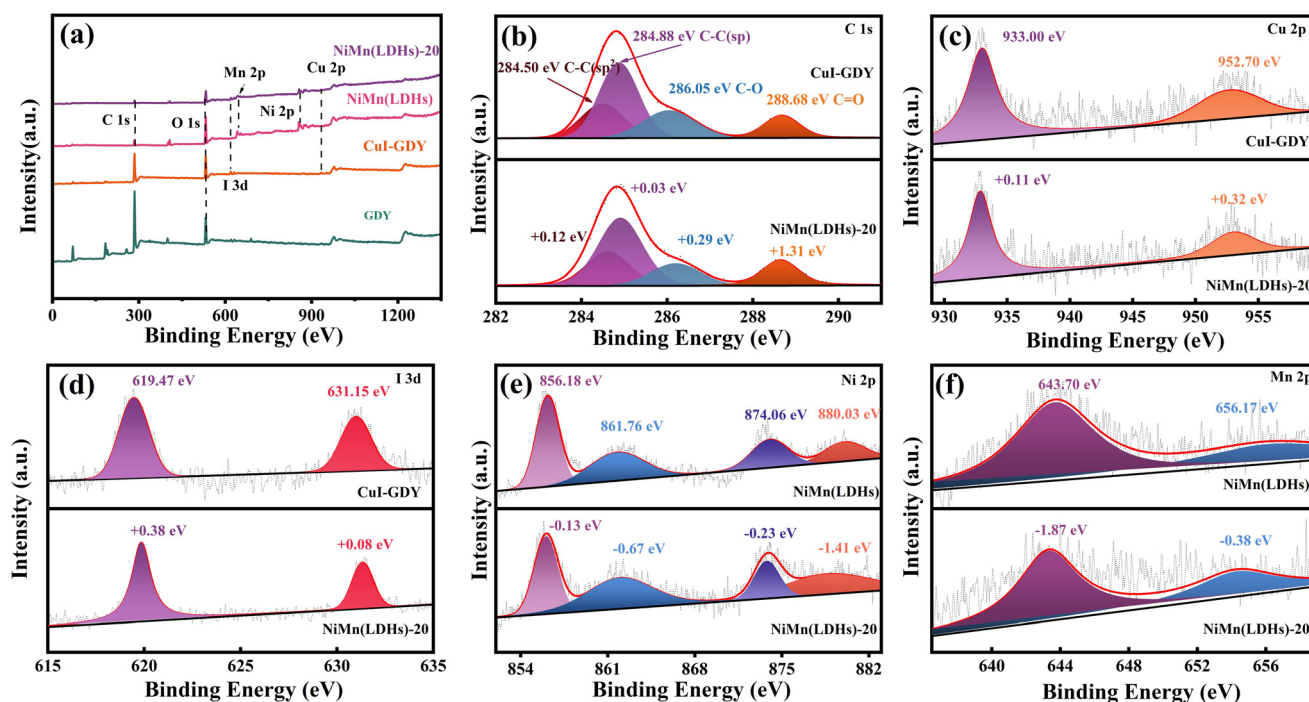

Fig. 5 XPS spectra of GDY, CuI–GDY, NiMn(LDHs), NiMn(LDHs)-20 (a), and survey spectra and high-resolution spectra of C 1s (b), Cu 2p (c), I 3d (d), Ni 2p (e), and Mn 2p (f).

3.4. SEM and TEM analysis

The microstructures and morphologies of CuI, GDY, CuI–GDY, NiMn(LDHs) and NiMn(LDHs)-20 were obtained by SEM. Fig. 6(a) shows the petal-like sheets stacked together in NiMn(LDHs). With a large specific surface area and rough surface, it is easy to load substances. Fig. 6(b and c) show the stone-like CuI and the layered stacked GDY. CuI is like stone and GDY is like cement, and the two are mixed together. This combination forms CuI–GDY, and its morphology can be seen in Fig. 6(d). In Fig. 6(e), two different aggregated states of CuI and NiMn(LDHs) are clearly visible. CuI–GDY is loaded on the rough surface of NiMn(LDHs), indicating the successful preparation of NiMn(LDHs)-20. Fig. 6(f) shows the TEM of the composite catalyst NiMn(LDHs)-20. The thick and poor light transmittance CuI particles, CuI–GDY generated by

the combination of CuI and villous GDY with border zone, and sheet-like NiMn(LDHs) can be observed from the TEM. Fig. 6(g and h) is the HRTEM diagram of the composite catalyst NiMn(LDHs)-20. We can see the lattice fringes (0.217 nm) belonging to the crystal plane of CuI (220), and (0.259 nm) belonging to the crystal plane of NiMn(LDHs) (012). Fig. 6(j) is the EDX detection result. The EDX results show that it contains Ni, Mn, C, O, I and Cu elements, which strongly proves the successful preparation of NiMn(LDHs)-20.

3.5. UV-vis DRS analysis

In general, the photocatalyst activity is positively correlated with the light absorption capacity of the photocatalyst.[46–48] The light absorption properties of the samples were tested using UV-vis diffuse reflectance spectroscopy, and the results
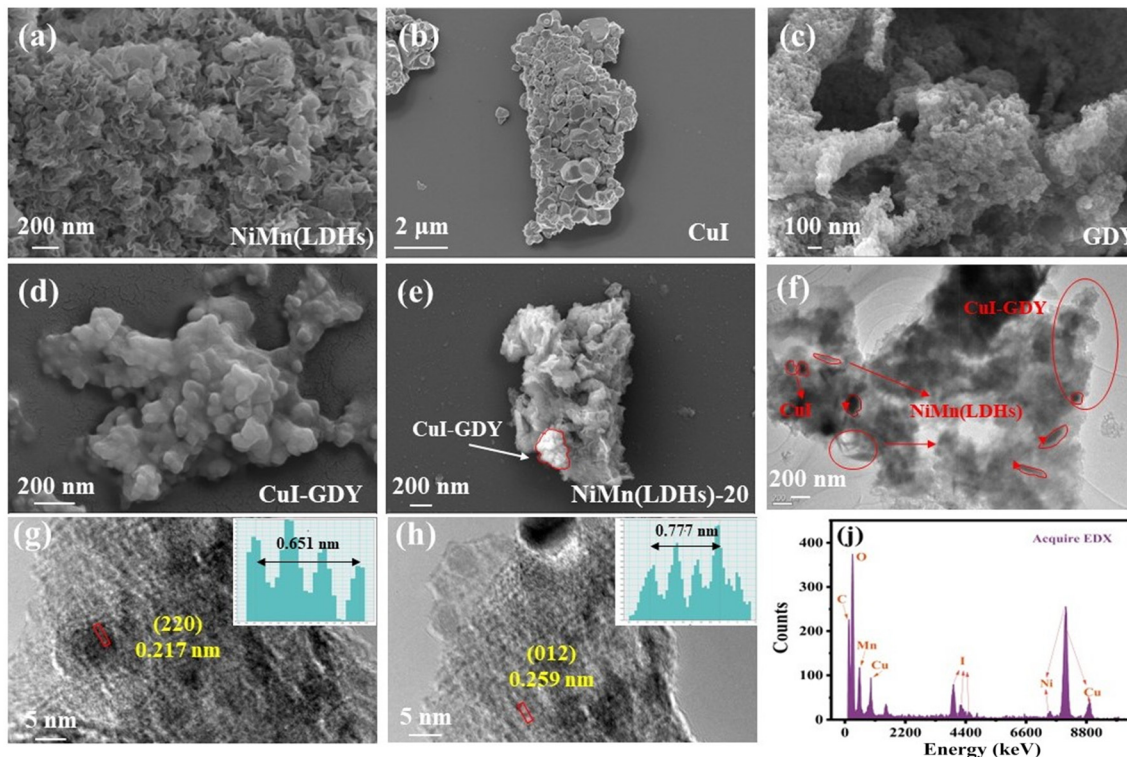
Fig. 6 (a–e) SEM of NiMn(LDHs), CuI, GDY, CuI–GDY, and NiMn(LDHs)-20. (f) TEM of NiMn(LDHs)-20, (g and h) HRTEM of NiMn(LDHS)-20, (j) and EDX of NiMn(LDHs)-20.

are shown in Fig. 7(a). GDY has good light absorption in the visible range. CuI has an obvious absorption band at 420 nm, which is still visible in NiMn(LDHs)-20, indicating the

success of the composite materials. Fig. 7(b) shows the light absorption intensity of GDY. As shown in Fig. 7(c), we then measured the apparent quantum efficiency (AQE) of the
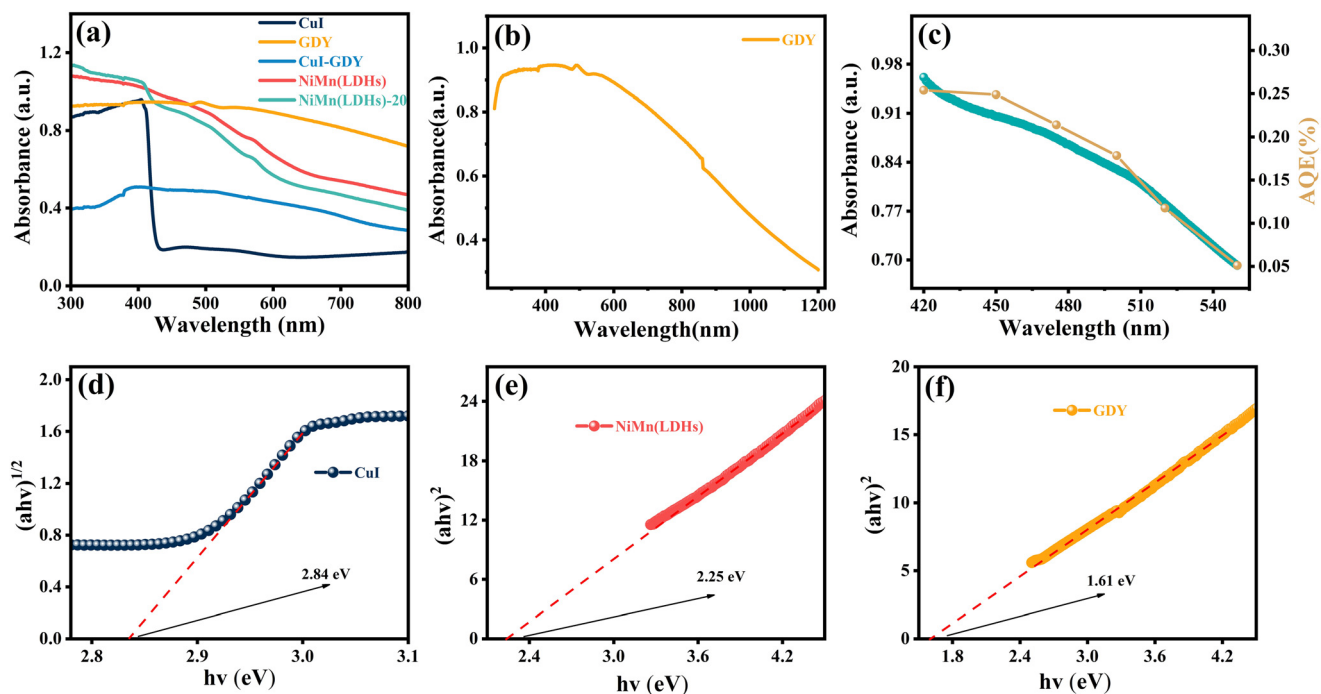
Fig. 7 (a) UV–vis diffuse reflectance spectra of CuI, GDY, CuI–GDY, NiMn(LDHs) and NiMn(LDHs)-20. (b) UV–vis diffuse reflectance spectra of GDY. (c) The apparent quantum efficiency of H_2 evolution for NiMn(LDHs)-20 under irradiation at different wavelengths (right axis), and the corresponding ultraviolet-visible spectrum (left axis) (d–f) and band gap energies of CuI, NiMn(LDHs) and GDY.

This journal is © The Royal Society of Chemistry 2023

Catal. Sci. Technol., 2023, **13**, 1074–1086 | **1079**

composite catalyst NiMn(LDHs)-20 (10 mg catalyst, 10 mg EY, 30 mL TEOA). The AQE was found to match the UV absorption curve of NiMn(LDHs)-20 well, which indicates that the catalyst has strong stability. Optical absorption is typically used to estimate the band gap of the prepared nanocatalysts.[49,50] Preliminary calculations for the band gap width of the catalyst can be made using the formula: $\alpha hv = A(hv - E_g)^{m/2}$, where α is the absorbance index, h is Planck's constant, v is the frequency, E_g is the semiconductor forbidden band width, A is a constant, and the value of m is related to whether the material has direct band gap ($m = 1$) or indirect band gap ($m = 4$).[51] As shown in Fig. 7(d–f), the E_g of CuI, NiMn(LDHs) and GDY are 2.84, 2.25 and 1.61 eV, respectively.

3.6. The PL and TRPL spectra

The photoluminescence properties of the catalysts were measured in EY solution. Simple EY and CuI–GDY produce strong fluorescence under light excitation, as shown in Fig. 9(a). This means that more excited electrons transformed by radiation decay return to the ground state.[52] As a result, the electron–hole recombination occurs faster, which counts against the hydrogen precipitation reaction. In all samples, the composite catalyst NiMn(LDHs)-20 has the lowest emission intensity. This is because the layered structure of NiMn(LDHs) has a large specific surface area, thus

facilitating the anchoring of CuI–GDY and speeding up the transfer of photogenerated electrons. More photogenerated electrons participate in the hydrogen evolution reaction and improve the utilization of photogenerated electrons. This corresponds to the catalytic activity of the samples. The peak intensities of EY, GDY, CuI–GDY, NiMn(LDHs), NiMn(LDHs)– CuI and NiMn(LDHs)-20 decrease successively, so the hydrogen production efficiency increases successively. To further research the interaction relationship between dye and catalyst, the lifetime of the samples was detected using fluorescence transients, and the results are shown in Table 1. The average lifetime, in particular, refers to the time it takes electrons to transition from the excited to the ground state. However, when CuI–GDY and NiMn(LDHs) are compounded, their average lifetime decreases significantly. This suggests that the electron transfer rate is accelerated, allowing more photogenerated electrons to participate in the hydrogen precipitation reaction. This increases the hydrogen production activity owing to the possible shape of the S-scheme heterojunction between the three.[53] A built-in electric field is formed inside the formed S-scheme heterojunction catalyst, providing an electron transfer channel. The Coulomb forces and energy band edge bending act to induce more useful electrons to participate in the reduction reaction.[54–56] To further demonstrate the formation of S-scheme heterojunctions between the composite catalysts, we calculated the electron transfer rates of the samples. The
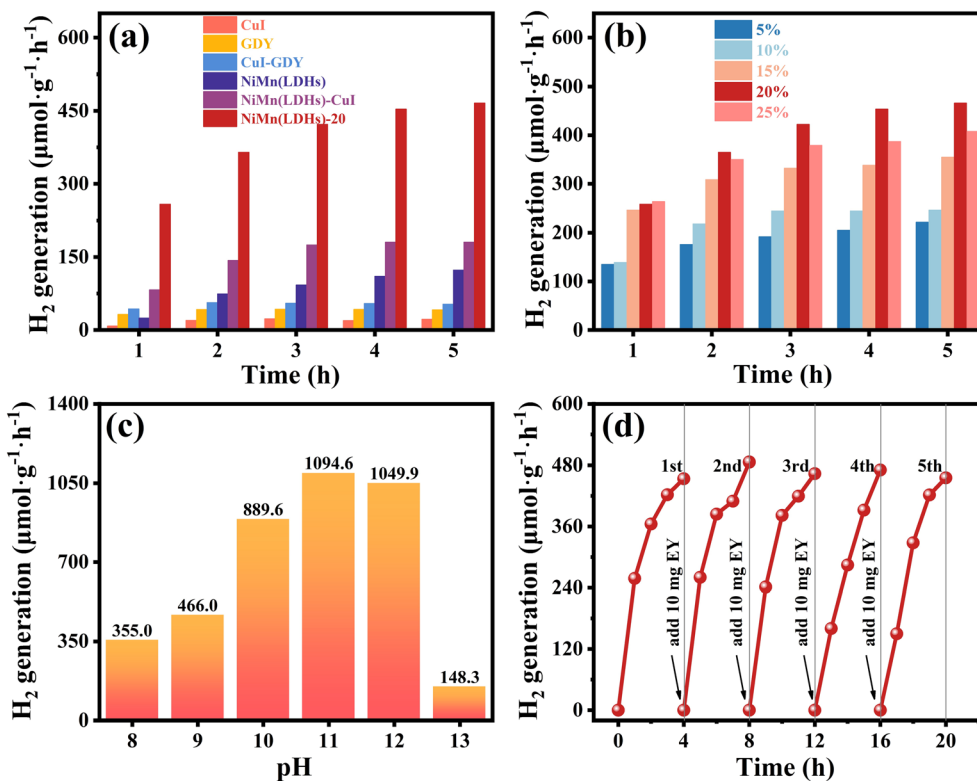

Fig. 8 (a) Time-dependent hydrogen production using different catalysts. (b) Hydrogen production activity of the NiMn(LDHs)-*x* (*x* = 5, 10, 15, 20, 25) composite catalyst. (c) Effect of the triethanolamine aqueous solution at different pH values on the photocatalytic activity of NiMn(LDHs)-20. (d) Cycling stability and regeneration test of the NiMn(LDHs)-20.
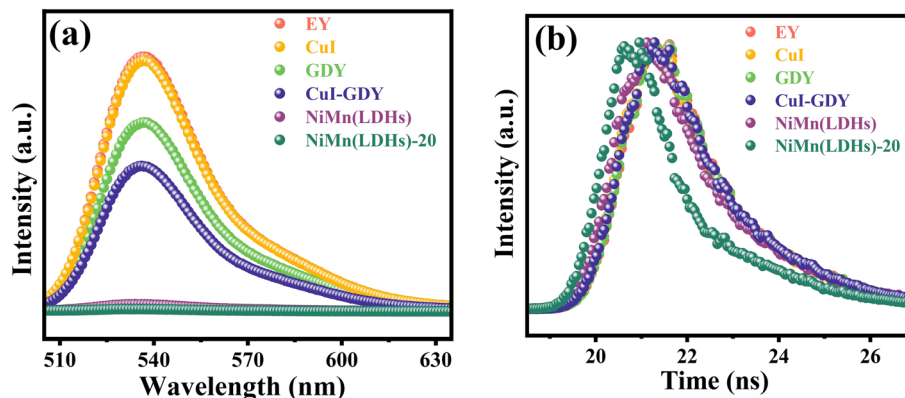
Fig. 9   (a) Steady-state fluorescence of the EY sensitization system and (b) transient fluorescence.

Table 1   Lifetimes and electron transfer rate of EY, CuI, GDY, CuI–GDY, NiMn(LDHs) and NiMn(LDHs)-20

Samples	τ_1 [ns]	τ_2 [ns]	τ_{ave} [ns]	k_{et} [10^9 s^{-1}]
EY	1.202 (100.00%)	—	1.202	0
CuI	0.991 (70.14%)	1.644 (29.86%)	1.125	0.057
GDY	1.082 (87.35%)	2.037 (12.65%)	1.150	0.039
NiMn(LDHs)	0.875 (52.31%)	1.673 (47.69%)	1.132	0.051
CuI–GDY	0.993 (66.82%)	1.683 (33.18%)	1.149	0.038
NiMn(LDHs)-20	1.457 (42.30%)	0.083 (57.70%)	0.139	6.362

average lifetime of the samples measured by steady-state fluorescence was used to calculate the electron transfer rate in the samples using the following equation:

$$k_{et} = \tau_{ave(sample)}^{-1} - \tau_{ave(EY)}^{-1}$$

The calculation results are shown in Table 1. We found that the electron transfer rate of the composite catalyst NiMn(LDHs)-20 was considerably faster compared with that of the single catalyst, suggesting the formation of the S-scheme heterojunctions between catalysts.[53]

3.7. Photocatalytic hydrogen evolution activity

The photocatalytic hydrogen production performance of the samples was investigated in a closed reaction system under visible light irradiation using a volume fraction of 15% and pH = 9 TEOA as a sacrificial reagent. As shown in Fig. 8(a), CuI, GDY, CuI–GDY, NiMn(LDHs)–CuI, pure NiMn(LDHs) and composite samples were used as catalysts to study the hydrogen production rate of the system. The hydrogen production rates of pure GDY, CuI, and NiMn(LDHs) are low. Furthermore, even the binary catalysts CuI–GDY and NiMn(LDHs)–CuI without GDY have average hydrogen production activity. When GDY is introduced to NiMn(LDHs), the hydrogen production rate is significantly increased. As shown in Fig. 8(b), when the content of CuI–GDY reaches 20%, the hydrogen evolution activity of the composite catalyst is at its best. However, when the content of CuI–GDY is greater than 20%, the hydrogen evolution activity of the composite catalyst decreases significantly. This result may

arise from the accumulation of excessive CuI–GDY, which prevents more light from reaching NiMn(LDHs).

Simultaneously, to study the activity of the composite catalyst in sacrificial reagents with different pH, the control test was set up to change only the pH of the sacrificial reagent to obtain the hydrogen production at each pH for 5 hours, as shown in Fig. 8(c). NiMn(LDHs)-20 has the best hydrogen evolution activity at pH = 11. The hydrogen production in 5 hours is 1094.6 µmol g^{-1} h^{-1}, which is about 2.3 times of that in Fig. 8(a). When pH = 12, the hydrogen production starts to decrease gradually. When it reaches pH = 13, the hydrogen production drops sharply. This is because the over alkaline environment will cause the oxidation degradation of TEOA to accelerate. On the other hand, the driving force for hydrogen production from water cleavage depends on the concentration of H$^+$ in the sacrificed reagent. Thus, there is a lower driving force for hydrogen production with increasing alkaline environment. However, this does not mean that a lower pH is better. A weak base environment that is close to neutral will protonate the sacrificial reagent so that it will provide fewer effective electrons. Thus, the hydrogen production activity will decrease, as shown in Fig. 8(c), when pH = 8. The results showed that to ensure the high activity of the catalyst, a sacrificial reagent with an appropriate pH value should be selected.

The catalyst should not be judged by the amount of hydrogen produced alone. The stability of the catalyst should also be taken into account. Therefore, we used 10 mg of EY in TEOA with pH = 9 to study the cyclic stability of the catalyst. As shown in Fig. 8(d), five cycles were performed for a total of 20 hours. TEOA was not replaced during the cycle.

However, 10 mg of EY was added in each cycle. Using N_2 to drain the gas in the bottle, there is only a slight decrease in the hydrogen production capacity of the catalyst at the end of each cycle. Therefore, the catalyst has strong cycle stability.

3.8. The electrochemical characterization test

Too often, the photocurrent response is an effective method to evaluate the capability of photogenerated carrier separation.[57] The photocurrent densities of different samples were tested under the same experimental conditions, and the test results are shown in Fig. 10(a). The pure GDY photocurrent density is the lowest. However, the photocurrent density of the composite NiMn(LDHs)–CuI is relatively higher because CuI and NiMn(LDHs) construct an S-scheme heterojunction to accelerate the transfer of photogenerated carriers.[58] Similarly, the composite catalyst showed the strongest photocurrent density compared with pure GDY and NiMn(LDHs). This indicates that the number of photogenerated carriers involved in recombination decreases, while the number of photogenerated carriers involved in hydrogen evolution reaction increases. This represents an increase in the utilization rate of generated photogenerated electrons, thus favoring hydrogen production.

The linear sweep voltammetry (LSV) results of the sample are shown in Fig. 10(b). NiMn(LDHs)-20 has the smallest current intensity in the same potential region, indicating that it has the smallest energy barrier and requires the least energy for the hydrogen evolution reaction. So, in the same

potential region, the lower the current intensity, the more favorable the hydrogen precipitation reaction.[59] Fig. 10(c) shows the electrochemical impedance spectroscopy (EIS) results of the sample. The electric arc radius can be used to determine the magnitude of the resistance during charge transfer at the interface between the working electrode and the electrolyte.[60–62] Furthermore, the composite catalyst NiMn(LDHs)-20 has the smallest electric arc radius, implying that charge transfer resistance is minimal. This indicates that the impedance of the composite catalyst composed of NiMn(LDHs) and CuI–GDY combined is greatly reduced. The greatly reduced impedance facilitates the transfer of photogenerated carriers and reduces the transfer time of photogenerated carriers, thus reducing the complexation of electron–hole pairs. This is favorable for the hydrogen evolution reaction.

The Mott–Schottky of CuI, NiMn(LDHs) and GDY were tested at 1000 Hz. It can be concluded as shown in Fig. 10(d–f) that the CuI, NiMn(LDHs) and GDY flat band potential (E_{fb}) are 0.08, 0.89 and −0.64 eV, respectively. It is known from the literature that CuI and GDY are n-type semiconductors. Based on the experimentally measured data, it is known that NiMn(LDHs) is a p-type semiconductor. In general, the conduction band potential (E_{CB}) of an n-type semiconductor is more negative (−0.1 or −0.2 eV) than its flat band potential, while the valence band potential (E_{VB}) of a p-type semiconductor is more positive (0.1 or 0.2 eV),[63] according to the formula $E_{NHE} = E_{SCE} + 0.24$, where E_{NHE} is the standard normal hydrogen electrode and E_{SCE} is the saturated calomel electrode potential.
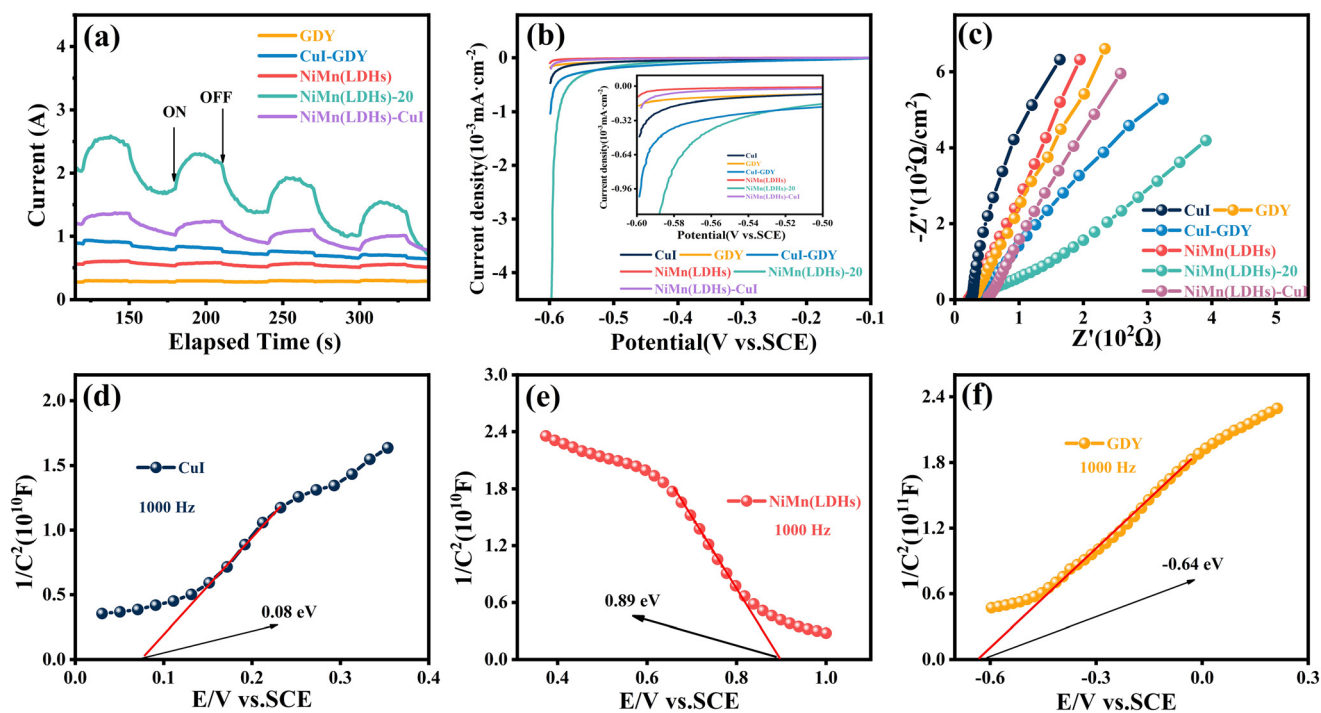

Fig. 10 (a) Transient photocurrent response of GDY, CuI–GDY, NiMn(LDHs), NiMn(LDHs)–CuI, NiMn(LDHs)-20; (b) LSV curves and (c) EIS spectra of CuI, GDY, CuI–GDY, NiMn(LDHs), NiMn(LDHs)–CuI, NiMn(LDHs)-20; (d–f) Mott–Schottky plots of CuI, NiMn(LDHs), and GDY.

1082 | *Catal. Sci. Technol.*, 2023, **13**, 1074–1086

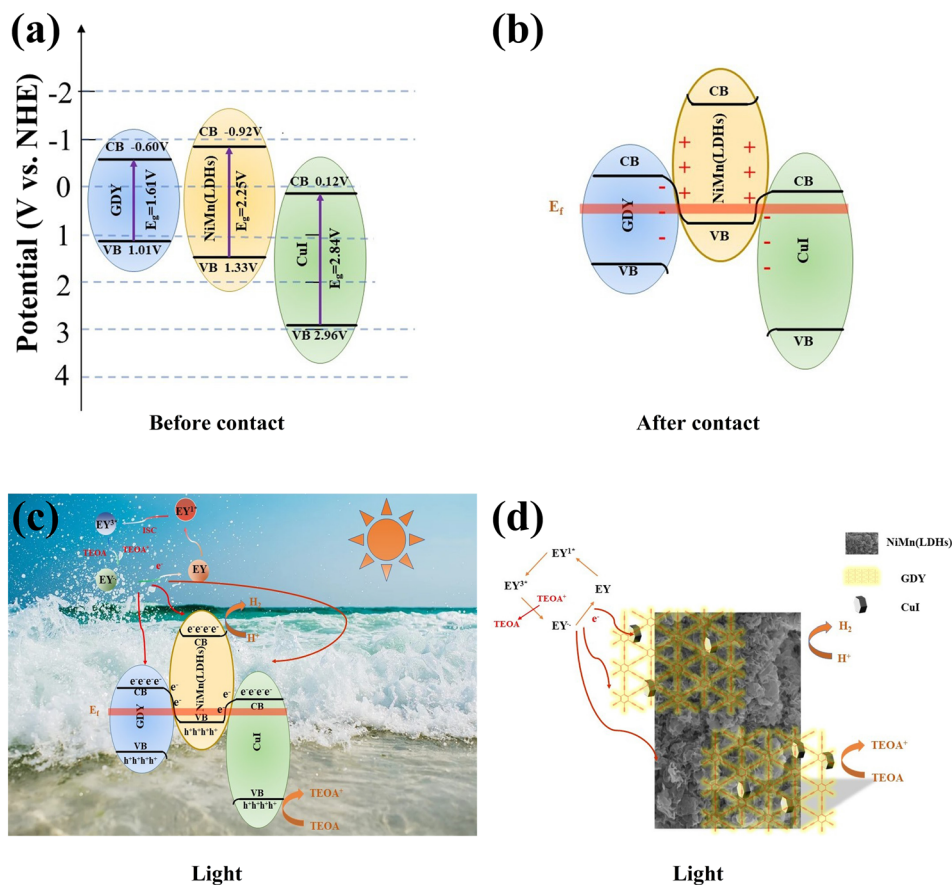This journal is © The Royal Society of Chemistry 2023

Fig. 11 (a and b) Double S-scheme heterojunction mechanism towards the charge transfer between CuI, GDY and NiMn(LDHs) before contact and after contact in darkness and under illumination. (c and d) Possible hydrogen evolution mechanism diagram for the GDY/CuI/NiMn(LDHs) photocatalyst.

Combined with the band gap measured in UV-vis, the conduction band (CB) and valence band (VB) information of the three catalysts can be obtained as shown in Fig. 11(a).

3.9. Proposed reaction mechanism

The possible hydrogen production mechanism of the CuI–GDY/NiMn(LDHs) composite catalyst was proposed based on the above contents. As shown in Fig. 11(a–d), first of all, when the catalyst contacts, the electrons in the NiMn(LDHs) valence band are transferred to GDY and CuI until the Fermi levels of the three are equal. At this time, NiMn(LDHs) becomes positively charged due to losing electrons, while GDY and CuI become negatively charged due to gaining electrons. Then EY is excited by visible light into a singly excited EY^{1*} state, and then converted to the more stable triple excited state EY^{3*} by intersystem transition (ISC). TEOA provides electrons to reduce EY^{3*} to a strongly reduced $EY^{\cdot-}$. Following that, $EY^{\cdot-}$ is transferred to the surface of the catalyst to participate in the hydrogen evolution reaction, while it is oxidized back to the ground state. When the composite catalyst is illuminated by light, the electrons on CB of GDY and CuI are closer to the hole on VB of NiMn(LDHs), so the electrons on CB of GDY and CuI are

more inclined to flow to the hole on VB of NiMn(LDHs), rather than combine with the hole itself. Thus, the electron–hole pair recombination of the semiconductor itself is reduced, and the hydrogen evolution ability is improved macroscopically.

4. Conclusion

In this paper, CuI–GDY was synthesized by an organic method, and CuI–GDY/NiMn(LDHs) nanocomposites were obtained by simple physical mixing. Under the action of CuI–GDY, the charge separation and transfer rate of NiMn(LDHs) in the mixed catalyst are significantly increased, and the recombination rate of the electron–hole pair is significantly inhibited. Under the condition of light, the hydrogen production rate reaches 1094.6 µmol g^{-1} h^{-1}, which is about 11.24, 8.80, 20.99, 3.78 and 2.58 times higher when compared to pure GDY, CuI–GDY, CuI, NiMn(LDHs) and NiMn(LDHs)–CuI. The double S-scheme heterojunctions constructed between the composite catalysts accelerate the electron transfer rate, resulting in more photogenerated electrons participating in the reduction of protons (H$^+$) at the active site. The good stability of GDY is brought to the composite catalyst after compounding. This causes the hole–electron

This journal is © The Royal Society of Chemistry 2023

Catal. Sci. Technol., 2023, **13**, 1074–1086 | **1083**

pair compounding rate of the composite catalyst to decrease, thus enabling the composite catalysts to maintain good hydrogen precipitation activity even after 20 hours of cycling, and further improves the hydrogen precipitation activity. This certainly provides a new idea for the application of CuI–GDY.

Author contributions

This experiment was designed by Zhenkun Liu. Zhenkun Liu performed the experiments; Zhiliang Jin provided reagents, materials, and analytical tools; Zhenkun Liu wrote the article.

Conflicts of interest

The authors declare no competing financial interest.

Acknowledgements

References

1 T. Yan, X. Zhang, H. Liu and Z. Jin, CeO_2 particles anchored to Ni_2P nanoplate for efficient photocatalytic hydrogen evolution, *Chin. J. Struct. Chem.*, 2022, **41**, 2201047–2201053.

2 J. Zhang, C. Cheng, F. S. Xing, C. Chen and C. Huang, 0D β-$Ni(OH)_2$ nanoparticles/1D $Mn_{0.3}Cd_{0.7}S$ nanorods with rich S vacancies for improved photocatalytic H_2 production, *Chem. Eng. J.*, 2021, **414**, 129157.

3 Y. Liu, X. Hao, H. Hu and Z. Jin, High efficiency electron transfer realized over $NiS_2/MoSe_2$ S-scheme heterojunction in photocatalytic hydrogen evolution, *Acta Phys.-Chim. Sin.*, 2021, **37**(6), 2008030.

4 Z. Jin, Y. Li and X. Hao, Ni, Co-based selenide anchored g-C_3N_4 for boosting photocatalytic hydrogen evolution, *Acta Phys.-Chim. Sin.*, 2021, **37**(10), 1912033.

5 S. Liu, K. Wang, M. Yang and Z. Jin, Rationally designed $Mn_{0.2}Cd_{0.8}S$@CoAl LDH S-scheme heterojunction for efficient photocatalytic hydrogen production, *Acta Phys.-Chim. Sin.*, 2022, **38**(7), 2109023.

6 H. Li, H. Gong and Z. Jin, In_2O_3-modified Three-dimensional nanoflower MoSx form S-scheme heterojunction for efficient hydrogen production, *Acta Phys.-Chim. Sin.*, 2022, **38**, 2201037.

7 G. Wang, Y. Quan, K. Yang and Z. Jin, EDA-assisted synthesis of multifunctional snowflake-Cu_2S/CdZnS S-Scheme heterjunction for improved the photocatalytic hydrogen evolution, *J. Mater. Sci. Technol.*, 2022, **121**, 28–39.

8 Z. Jiang, Q. Chen, Q. Zheng, R. Shen, P. Zhang and X. Li, Constructing 1D/2D schottky-based heterojunctions between $Mn_{0.2}Cd_{0.8}S$ Nanorods and Ti_3C_2 nanosheets for boosted photocatalytic H_2 evolution, *Acta Phys.-Chim. Sin.*, 2021, **37**(6), 2009063.

9 Z. Fan, X. Guo, Z. Jin, X. Li and Y. Li, Bridging effect of S-C bond for boosting electron transfer over cubic hollow CoS/g-C_3N_4 heterojunction toward photocatalytic hydrogen production, *Langmuir*, 2022, **38**(10), 3244–3256.

10 F. Yang, X. Chua, J. Sun, Y. Zhang, Z. Li, H. Liu, L. Bai, Q. Yang and L. Jing, Efficient singlet oxygen generation by excitonic energy transfer on ultrathin g-C_3N_4 for selective photocatalytic oxidation of methyl-phenyl-sulfide with O_2, *Chin. Chem. Lett.*, 2020, **31**, 2784–2788.

11 R. Yan, A. Zada, L. Sun, Z. Li, Z. Mu, S. Chen, F. Yang, J. Sun, L. Bai, Y. Qu and L. Jing, Comparative study of metal oxides and phosphate modification with different mechanisms over g-C_3N_4 for visible-light photocatalytic degradation of Metribuzin, *Rare Met.*, 2022, **41**, 155–165.

12 Y. Wang, Y. Qu, B. Qu, L. Bai, Y. Liu, Z. Yang, W. Zhang, L. Jing and H. Fu, Construction of Six-Oxygen-Coordinated Single Ni Sites on g-C_3N_4 with Boron-Oxo Species for Photocatalytic Water-Activation-Induced CO_2 Reduction, *Adv. Mater.*, 2021, **33**, 2105482.

13 X. Li, K. Pan, Y. Qu and G. Wang, One dimension carbon self-doping g-C_3N_4 nanotubes: synthesis and application in dye-sensitized solar cells, *Nano Res.*, 2018, **11**(3), 1322–1330.

14 Y. Cao, H. Gou, P. Zhu and Z. Jin, Ingenious design of CoAl-LDH p-n heterojunction based on CuI as holes receptor for photocatalytic hydrogen evolution, *Chin. J. Struct. Chem.*, 2022, **41**, 2206079–2206085.

15 J. Zou, G. Liao, J. Jiang, Z. Xiong, S. Bai, H. Wang, P. Wu and P. Zhang, In-situ Construction of Sulfur-doped g-C_3N_4/defective g-C_3N_4 Isotype Step-scheme Heterojunction for Boosting Photocatalytic H_2 Evolution, *Chin. J. Struct. Chem.*, 2022, **41**, 2201025–2201033.

16 Z. Jin, T. Li, L. Zhang, X. Wang, G. Wang and X. Hao, Construction of a tandem S-scheme GDY/CuI/CdS-R heterostructure based on morphology-regulated graphdiyne (g-C_nH_{2n-2}) for enhanced photocatalytic hydrogen evolution, *J. Mater. Chem. A*, 2022, **10**, 1976–1991.

17 Z. Jin and H. Gong, A New Allotrope of Carbon—Graphdiyne (g-C_nH_{2n-2}) Boosting with $Mn_{0.2}Cd_{0.8}S$ form S-Scheme Heterojunction for Efficient Photocatalytic Hydrogen Evolution, *Adv. Mater. Interfaces*, 2021, **8**, 2100630.

18 D. Ren, R. Shen, Z. Jiang, X. Lu and X. Li, Highly efficient visible-light photocatalytic H_2 evolution over 2D-2D CdS/Cu_7S_4 layered heterojunctions, *Chin. J. Catal.*, 2020, **41**, 31–40.

19 R. Shen, Y. Ding, S. Li, P. Zhang, Q. Xiang, Y. Hau and X. Li, Constructing low-cost Ni_3C/twin-crystal $Zn_{0.5}Cd_{0.5}S$ heterojunction/homojunction nanohybrids for efficient photocatalytic H_2 evolution, Chinese, *Chin. J. Catal.*, 2021, **42**, 25–36.

20 Y. Liu, M. Lu, T.-P. Perng and L.-J. Chen, Plasmonic enhancement of hydrogen production by water splitting with CdS nanowires protected by metallic TiN overlayers as highly efficient photocatalysts, *Nano Energy*, 2021, **89**, 106407.

21 J. Qin, X. Hua, X. Li, Z. Yin, B. Liu and K.-H. Lam, 0D/2D $AgInS_2$/MXene Z-scheme heterojunction nanosheets for

1084 | *Catal. Sci. Technol.*, 2023, **13**, 1074–1086

This journal is © The Royal Society of Chemistry 2023

improved ammonia photosynthesis of N_2, *Nano Energy*, 2019, **61**, 27–35.

22 S. Wageh, A. A. Al-Ghamdi, R. Jafer, X. Li and P. Zhang, A new heterojunction in photocatalysis: S-scheme heterojunction, *Chin. J. Catal.*, 2021, **42**, 667–669.

23 J. Wei, Y. Chen, H. Zhang, Z. Zhuang and Y. Yan, Hierarchically porous S-scheme CdS/UiO-66 photocatalyst for efficient 4-nitroaniline reduction, *Chin. J. Catal.*, 2021, **42**, 78–86.

24 J. Peng, J. Shen, X. Yu, H. Tang, Zulfiqar and Q. Liu, Construction of LSPR-enhanced 0D/2D CdS/MoO_{3-x} S-scheme heterojunctions for visible-light-driven photocatalytic H_2 evolution, *Chin. J. Catal.*, 2021, **42**, 87–96.

25 Y. Fang, Y. Liu, L. Qi, Y. Xue and Y. Li, 2D graphdiyne: an emerging carbon material, *Chem. Soc. Rev.*, 2022, **51**, 2681–2709.

26 G. Li, Y. Li, H. Liu, Y. Guo, Y. Li and D. Zhu, Architecture of graphdiyne nanoscale films, *Chem. Commun.*, 2010, **46**, 3256–3258.

27 Z. Zuo, F. He, F. Wang, L. Li and Y. Li, Spontaneously Splitting Copper Nanowires into Quantum Dots on Graphdiyne for Suppressing Lithium Dendrites, *Adv. Mater.*, 2020, **32**, 2004379.

28 X. Qian, Z. Ning, Y. Li, H. Liu, C. Ouyang, Q. Chen and Y. Li, Construction of graphdiyne nanowires with high-conductivity and mobility, *Dalton Trans.*, 2012, **41**, 730–733.

29 Y. Zhao, J. Wan, H. Yao, L. Zhang, K. Lin, L. Wang, N. Yang, D. Liu, L. Song, J. Zhu, G. Lin, L. Liu, H. Zhao, Y. Li and D. Wang, Few-layer graphdiyne doped with sp-hybridized nitrogen atoms at acetylenic sites for oxygen reduction electrocatalysis, *Nat. Chem.*, 2018, **10**, 924–931.

30 J. Yang, C. Yu, X. Fan, J. Qiu, J. Yang, C. Yu, X. Fan and J. Qiu, 3D Architecture Materials Made of NiCoAl-LDH Nanoplates Coupled with NiCo-Carbonate Hydroxide Nanowires Grown on Flexible Graphite Paper for Asymmetric Supercapacitors, *Adv. Energy Mater.*, 2014, **4**, 1400761.

31 J. Chen, X. Wang, J. Wang and P. S. Lee, Sulfidation of NiMn-Layered Double Hydroxides/Graphene Oxide Composites toward Supercapacitor Electrodes with Enhanced Performance, *Adv. Energy Mater.*, 2016, **6**, 1501745.

32 M. Li, P. Yuan, S. Guo, F. Liu and J. P. Cheng, Design and synthesis of Ni-Co and Ni-Mn layered double hydroxides hollow microspheres for supercapacitor, *Int. J. Hydrogen Energy*, 2017, **42**, 28797–28806.

33 Z. Fan, X. Zhang, Y. Li, X. Guo and Z. Jin, Construct 3D NiCo-LDH/Cu_2O p-n heterojunction via electrostatic self-assembly for enhanced photocatalytic hydrogen evolution, *J. Ind. Eng. Chem.*, 2022, **110**, 491–502.

34 Y. Wu, Y. Li, L. Zhang and Z. Jin, NiAl-LDH in situ derived Ni_2P and ZnCdS nanoparticles ingeniously constructed S-scheme heterojunction for photocatalytic hydrogen production, *ChemCatChem*, 2022, **14**, e202101656.

35 M. Yu, R. Liu, J. Liu, S. Li and Y. Ma, Polyhedral-Like NiMn-Layered Double Hydroxide/Porous Carbon as Electrode for Enhanced Electrochemical Performance Supercapacitors, *Small*, 2017, **13**, 1702616.

36 Z. Jin, Y. Li and Q. Ma, CoAl LDH@Ni-MOF-74 S-Scheme Heterojunction for Efficient Hydrogen Evolution, *Trans. Tianjin Univ.*, 2021, **27**, 127–138.

37 D. Li, X. Ma, P. Su, S. Yang, Z. Jiang, Y. Li and Z. Jin, Effect of phosphating on NiAl-LDH layered double hydroxide form S-scheme heterojunction for photocatalytic hydrogen evolution, *Mol. Catal.*, 2021, **516**, 111990.

38 Y. Li, H. Yang, G. Wang, B. Ma and Z. Jin, Distinctive Improved Synthesis and Application Extensions Graphdiyne for Efficient Photocatalytic Hydrogen Evolution, *ChemCatChem*, 2020, **12**, 1985–1995.

39 Z. Jin, H. Li and J. Li, Efficient photocatalytic hydrogen evolution over graphdiyne boosted with a cobalt sulfide formed S-scheme heterojunctions, *Chin. J. Catal.*, 2022, **42**, 303–315.

40 Q. Xu, B. Zhua, B. Cheng, J. Yu, M. Zhou and W. Ho, Photocatalytic H_2 Evolution on Graphdiyne/$g-C_3N_4$ Hybrid Nano-composites, *Appl. Catal., B*, 2019, **255**, 117770.

41 K. Yang, T. Liu, D. Xiang, Y. Li and Z. Jin, Graphdiyne ($g-C_nH_{2n-2}$) based Co_3S_4 anchoring and edge-covalently modification coupled with carbon-defects $g-C_3N_4$ for photocatalytic hydrogen production, *Sep. Purif. Technol.*, 2022, **298**, 121564.

42 Y. Jia, L. Zhang, A. Du, G. Gao, J. Chen, X. Yan, C. L. Brown and X. Yao, Defect Graphene As a Trifunctional Catalyst for Electrochemical Reactions, *Adv. Mater.*, 2016, **28**, 9532–9538.

43 A. C. Ferrari, J. C. Meyer, V. Scardaci, C. Casiraghi, M. Lazzeri, F. Mauri, S. Piscanec, D. Jiang, K. S. Novoselov, S. Roth and A. K. Geim, Raman Spectrum of Graphene and Graphene Layers, *Phys. Rev. Lett.*, 2006, **97**, 187401.

44 Z. Jin, L. Zhang, G. Wang, Y. Li and Y. Wang, Graphdiyne Formed a Novel CuI-GD/$g-C_3N_4$ S-scheme Hetero-junction Composite for Efficient Photocatalytic Hydrogen Evolution, *Sustain*, *Sustain. Energy Fuels*, 2020, **4**, 5088–5101.

45 N. Yamada, R. Ino and Y. Ninomiya, Truly Transparent p-Type γ-CuI Thin Films with High Hole Mobility, *Chem. Mater.*, 2016, **28**, 4971–4981.

46 H. Gong, Y. Li, H. Li and Z. Jin, 2D CeO_2 and partial phosphated 2D Ni-based metal-organic framework formed S-scheme heterojunction for efficient photocatalytic hydrogen evolution, *Langmuir*, 2022, **38**, 2117–2131.

47 J. Li, M. Li, Y. Li, X. Guo and Z. Jin, Lotus-leaf-like $Bi_2O_2CO_3$ nanosheet combined with Mo_2S_3 for higher photocatalytic hydrogen evolution, *Sep. Purif. Technol.*, 2022, **288**, 120588.

48 R. Gao, H. He, J. Bai, L. Hao, R. Shen, P. Zhang, Y. Li and X. Li, Pyrene-benzothiadiazole-based Polymer/CdS 2D/2D Organic/Inorganic Hybrid S-scheme Heterojunction for Efficient Photocatalytic H_2 Evolution, *Chin. J. Struct. Chem.*, 2022, **41**, 2206031–2206038.

49 L. Zhang, X. Hao, Y. Li and Z. Jin, Performance of WO3/g-C3N4 heterojunction composite boosting with NiS for photocatalytic hydrogen evolution, *Appl. Surf. Sci.*, 2020, **499**, 143862.

50 B. Wang, S. He, W. Feng, L. Zhang, X. Huang, K. Wang, S. Zhang and P. Liu, Rational design and facile in situ coupling non-noble metal Cd nanoparticles and CdS nanorods for

This journal is © The Royal Society of Chemistry 2023

Catal. Sci. Technol., 2023, **13**, 1074–1086 | **1085**

efficient visible-light-driven photocatalytic H_2 evolution, *Appl. Catal., B*, 2018, **236**, 233–239.

51 Y. Wang, X. Hao, L. Zhang, Z. Jin and T. Zhao, Amorphous Co3S4 Nanoparticle-Modified Tubular g-C_3N_4 forms Step-scheme Heterojunctions for Photocatalytic Hydrogen Production, *Catal. Sci. Technol.*, 2021, **11**, 943–955.

52 J. Tian, Q. Liu, N. Cheng, A. M. Asiri and X. Sun, Self-Supported Cu_3P Nanowire Arrays as an Integrated High-Performance Three-Dimensional Cathode for Generating Hydrogen from Water, *Angew. Chem.*, 2014, **126**, 9731–9735.

53 Q. Xu, L. Zhang, B. Cheng, J. Fan and J. Yu, S-Scheme Heterojunction Photocatalyst, *Chem*, 2020, **6**, 1543–1559.

54 A. Meng, B. Cheng, H. Tan, J. Fan, C. Su and Y. Jiaguo, TiO_2/polydopamine S-scheme heterojunction photocatalyst with enhanced CO_2-reduction selectivity, *Appl. Catal., B*, 2021, **289**, 120039.

55 X. Han, B. Lu, X. Huang, C. Liu, S. Chen, J. Chen, Z. Zeng, S. Deng and J. Wang, Novel p- and n-type S-scheme heterojunction photocatalyst for boosted CO_2 photoreduction activity, *Appl. Catal., B*, 2022, **316**, 121587.

56 L. Chen, X. Song, J. Ren and Z. Yuan, Precisely modifying Co_2P/black TiO_2 S-scheme heterojunction by in situ formed P and C dopants for enhanced photocatalytic H_2 production, *Appl. Catal., B*, 2022, **315**, 121546.

57 L. Zhang, X. Hao, Q. Jian and Z. Jin, Ferrous oxalate dehydrate over CdS as Z-scheme photocatalytic hydrogen evolution, *J. Solid State Chem.*, 2019, **274**, 286–294.

58 Z. Jin, X. Wang, X. Hao, G. Wang, X. Guo and K. Wang, Graphdiyne based GDY/CuI/NiO parallel double S-scheme heterojunction for efficient photocatalytic hydrogen evolution, *2D Mater.*, 2022, **9**, 025014.

59 T. Yan, H. Liu and Z. Jin, Graphdiyne based ternary GD-CuI-$NiTiO_3$ S-scheme heterojunction photocatalyst for hydrogen evolution, *ACS Appl. Mater. Interfaces*, 2021, **13**, 24896–24906.

60 J. Fu, Q. Xu, J. Low, C. Jiang and J. Yu, Ultrathin 2D/ 2D WO_3/g-C_3N_4 Step-scheme H_2-Production Photocatalyst, *Appl. Catal., B*, 2019, **243**, 556–565.

61 F. He, A. Meng, B. Cheng, W. Ho and J. Yu, Enhanced Photocatalytic H_2-Production Activity of WO_3/TiO_2 Step-scheme Heterojunction by Graphene Modification, *Chin. J. Catal.*, 2020, **41**, 9–20.

62 W. Zhang, Y. Zou, X. Mei, Y. Li, S. Peng and J. Xu, Facile Synthesis of $Co_2(OH)_3Cl$/Cobalt Carbide/Reduced Graphene Oxide Composites for Enhanced Dye-Sensitized Photocatalytic H_2 Evolution, Sustain, *Sustain. Energy Fuels*, 2020, **4**, 6181–6187.

63 L. Zhang, X. Hao, J. Li, Y. Wang and Z. Jin, Unique synergistic effects of ZIF-9(Co)-derived cobalt phosphide and $CeVO_4$ heterojunction for efficient hydrogen evolution, *Chin. J. Catal.*, 2020, **41**, 82–94.

1086 | *Catal. Sci. Technol.*, 2023, **13**, 1074–1086

This journal is © The Royal Society of Chemistry 2023